RESEARCH

Parameter evaluation method of tight carbonate reservoir using electrical imaging pores diameter spectrum

Shixiang Jiao · Jun Zhao · Xiaofeng Ren · Xiaofeng Wen · Anpei Liu · Fang Cai · Baocai Yu · Qiang Lai

Abstract Currently, high-yield gas reservoirs have been discovered by exploring Lower Paleozoic tight carbonate oil and gas reservoirs in the Changqing area. These reservoirs, however, are impacted by subsequent karstification and diagenesis processes, leading to the formation of complex pore spaces with varying pore diameters ranging from microns to millimeters. Conventional well curves, with a resolution at the decimeter level, can only provide an overview of the reservoir porosity, making it challenging to evaluate the pore structure. On the other hand, electrical imaging logging data has a sampling interval of 0.1 inches and a resolution as fine as 5 mm, providing valuable information for pore structure evaluation in tight reservoirs. Since formation resistivity is influenced by factors like porosity, mud filtrate resistivity, and cementation, the cementation index serves as a reflection of the pore structure. Therefore, by calibrating the cementation index using data obtained from experiments at different scales, the pore structure parameters of tight carbonate reservoirs can be evaluated. This study conducted a comparison between numerous core experiments at various scales and both conventional and imaging log data. A method was proposed for extracting pore size distribution characteristics and calculating the pore size spectrum based on electrical imaging logging, ultimately leading to the establishment of a quantitative evaluation model for the pore structure of tight carbonate reservoirs. The results demonstrated improved accuracy and consistency in interpretation, as confirmed by well test data.

S. Jiao · J. Zhao (✉)
School of Geoscience and Technology, Southwest Petroleum University, Chengdu 610500, People's Republic of China
e-mail: zhaojun_70@126.com

S. Jiao
e-mail: cwbp.sunshinej@gmail.com

S. Jiao · J. Zhao
State Key Laboratory of Oil and Gas Reservoir Geology and Exploitation, Southwest Petroleum University, Chengdu 610500, People's Republic of China

S. Jiao · J. Zhao
Natural Gas Geology Key Laboratory of Sichuan Province, Southwest Petroleum University, Chengdu 610500, People's Republic of China

X. Ren · X. Wen · A. Liu · F. Cai · B. Yu
Changqing Branch, China national logging corporation, Xi'an, Shaanxi 710200, People's Republic of China

Q. Lai
Exploration and Development Research Institute, PetroChina Southwest Oil and Gas Field Company, Chengdu 610000, People's Republic of China

Highlights

1. The functional relationship between the cementation index and pore size is established based on

experimental analysis data from cores at various scales.

2. Taking into consideration the contribution of different pore components to permeability, we have proposed the pore component method for calculating reservoir permeability.

3. By conducting a comprehensive comparison of numerous core experiments, conventional logging, imaging logging, and other data, this paper presents a method for extracting pore size distribution features and calculating the pore size spectrum based on electrical imaging logging.

- The coal wall breakage deflection formula is constructed.
- Bracket horizontal force has an effect on coal wall breakage.
- The regression equation between the bracket support parameter and the index of plasticity zone occupancy is established.
- Adjusting support parameters can prevent coal wall rib spalling to a certain extent.
- Increasing support resistance at the working face is beneficial to the stability control of coal wall.

1 Introduction

The Ordos Basin is renowned for its extensive exploration opportunities and abundant oil and gas resources (Yang et al. 2005; Jingli et al. 2013; Liu 1998). Since the "10th Five-Year Plan", it has been the primary area for discovering new reserves in our country. Currently, there has been a significant breakthrough in the discovery of high-yield gas reservoirs in the Lower Paleozoic tight carbonate rock of the Changqing Oilfield. However, these oil reservoirs exhibit diverse storage space types and complex development. The pores within these reservoirs consist of micropores, fine pores, mesopores, macropores, and cavities. Intergranular dissolved pores of various scales, ranging from micrometers to millimeters, are commonly observed (Jinhua et al. 2019).

Traditional well logging data presents challenges in evaluating the pore structure parameters of tight carbonate reservoirs (Chen et al. 2020). In contrast, electrical imaging logging data offers wide coverage, high resolution, and continuous information (Zhang et al. 2018; Chitale et al. 2004; Chong et al. 2019; Feng 2019; Safinya et al. 1991). Although several methods have been proposed to interpret electroimaging log data, they heavily rely on the interpreter's expertise, making quantitative evaluation of tight carbonate reservoirs without core data difficult (Haizhou et al. 2016). To minimize subjective factors and enhance the accuracy of evaluating reservoir pore structure parameters, it is crucial to extract characteristic parameters from electrical imaging logging data for the quantitative assessment of tight carbonate reservoir parameters.

Conventional well logs are capable of assessing the porosity of carbonate reservoirs; however, they can only provide an overall view of the reservoir's porosity. When it comes to tight carbonate salt reservoirs with pore sizes mainly in the millimeter range, the resolution of conventional well logging curves is inadequate for evaluating the pore structure of such reservoirs. On the other hand, electrical imaging logging offers unique advantages compared to traditional logging methods. It provides high-resolution, 360-degree images around the well, enabling visualization of lithology and physical properties of the surrounding formations through environmentally corrected color changes. Typically, electrical imaging logging is utilized in geological research, structural analysis, and deposition (Jianping et al. 2011; Wu et al. 2013). While numerous researchers and experts have examined the application of electrical imaging logging data in reservoir evaluation (Khoshbakht et al. 2012; Xu et al. 2021), there is a dearth of research on utilizing this data to calculate reservoir pore structure and permeability parameters.

The study discovered that even when carbonate reservoir cores in the study area exhibit similar porosity, there are substantial differences in permeability. This implies that permeability is not solely determined by porosity, but is also influenced by factors such as pore type, pore size distribution, and connectivity. Electric imaging logging data has a sampling interval of 0.1 inches and a resolution of up to 5 mm. It can characterize pore information in the formation at the micron to millimeter scale. Following calibration with core

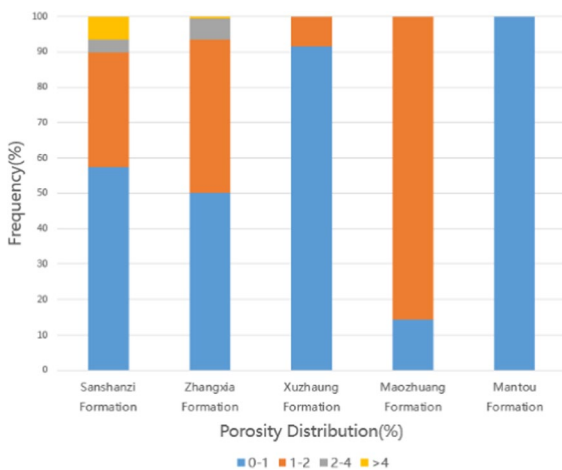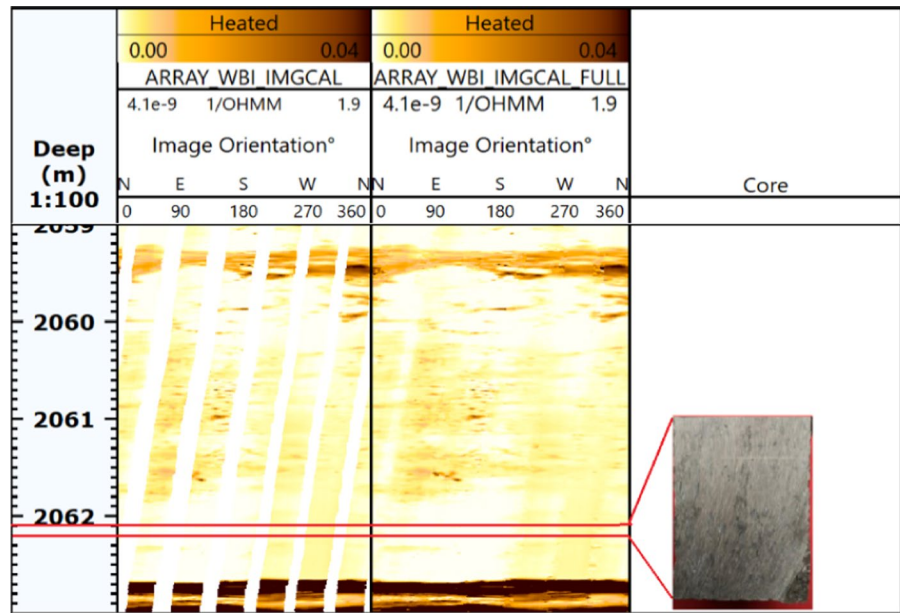**Fig. 1** Comparison of electrical imaging image and core at 2062.1~2062.2 m in MI x well
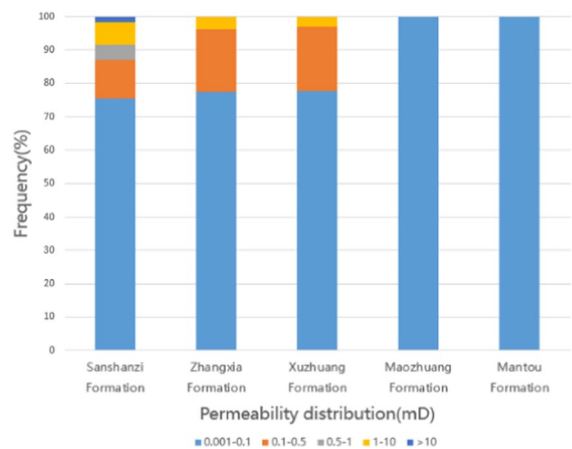

Fig. 2 Porosity distribution map

Fig. 3 Permeability distribution map

experimental data, factors impacting permeability can be directly analyzed. Furthermore, a quantitative identification of the spatial distribution and internal geometric structure of carbonate reservoir pores holds immense significance for well logging evaluation. The aspiration is that calculating reservoir pore structure and permeability parameters through electrical imaging data can significantly address the limitations associated with logging evaluation of tight carbonate reservoirs.

2 Reservoir characteristics

The lithology of Cambrian carbonate reservoir in Ordos Basin is dominated by micrite and silty dolomite, while the karst residual hill type gas reservoir is widely developed in the reservoir. Calcite and argillaceous filling degree is high, and the lithology is dense. Therefore, it is difficult to directly display the degree of pores development by electrical imaging. Taking well Mi x as an example (Fig. 1) with the logging depth of 2062.1 m, the core analysis shows

that the lithology is silty dolomite, the porosity is 2%, the permeability is 0.023 md, while the development degree of secondary porosity is low. Electrical imaging shows that the resistivity is high and the degree of pores development is very low. Thus, it is difficult to analyze the porosity and permeability parameters of the reservoir from the electrical imaging map.
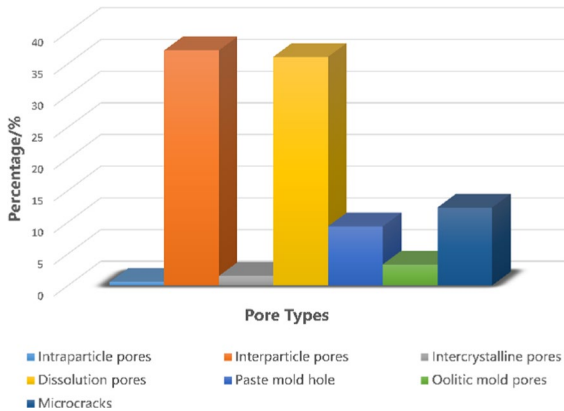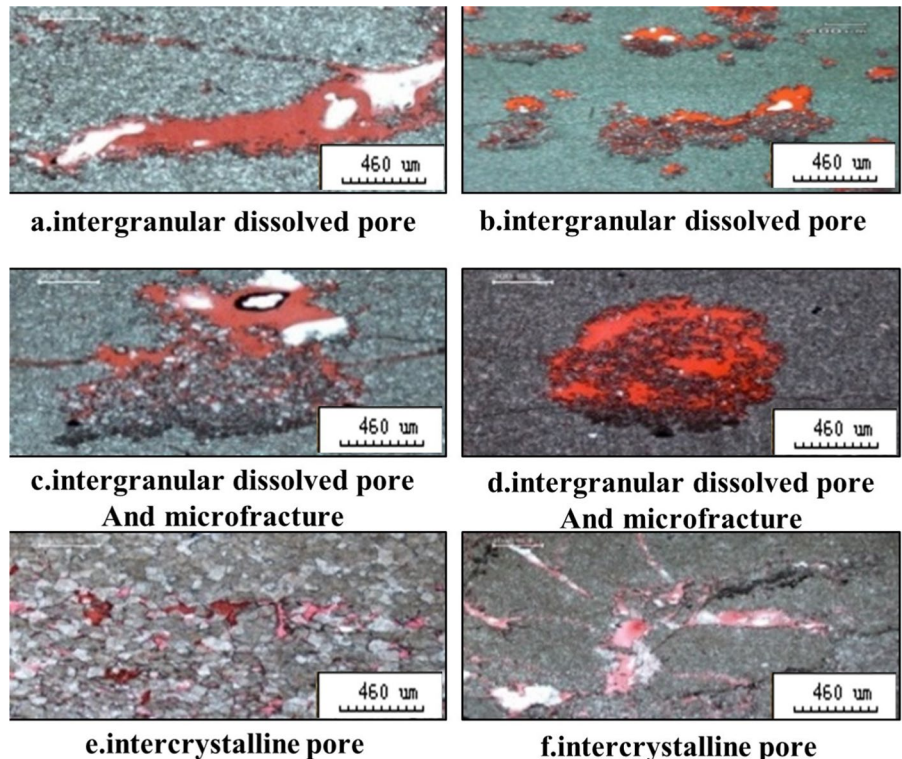
According to the analysis of 768 blocks of Cambrian reservoir samples, the statistical porosity ranges from 0.03% to 14.15% (Fig. 2). During the Maozhuang formation, the main distribution range of porosity is 0%~1%, while the Maozhuang formation distribution range is 1%~2% and the average porosity of the reservoir is 0.97%. We considered 735 permeability analysis samples, ranging from 0.002 to 33.5 md (Fig. 3). The main permeability distribution range is 0.001~0.1 md and the average permeability of the reservoir is 0.47 md. Furthermore, the samples with porosity < 1%, account for 62.59%; the samples with permeability < 0.1 md account for 80.71%; while the samples with permeability > 10 md is observed. The reservoir physical property is generally very poor, and the permeability does not increase with the increase in porosity. The overall performance is "low porosity-low permeability" pores type seepage characteristics and "low porosity-medium high permeability" fracture type seepage characteristics locally.

The pores types in 272 samples of 24 wells in the study area were analyzed statistically. Based on the analysis, we discovered that the pores of the reservoir in the Mawu subsection were intergranular pores,

Fig. 4 Distribution of pores types

Fig. 5 Thin sections of pore types

a.intergranular dissolved pore

b.intergranular dissolved pore

c.intergranular dissolved pore And microfracture

d.intergranular dissolved pore And microfracture

e.intercrystalline pore

f.intercrystalline pore

dissolution pores, and micro fractures. Dissolution pores were the main reservoir space, accounting for 73.14% of the total pores gap (Fig. 4). The reservoir space types were mainly intergranular pores type reservoirs (Fig. 5). This is because the pores diameter of the intergranular pores is generally in the micron level. It is difficult to directly judge the current pores diameter distribution range from the electrical imaging image. Therefore, this paper uses the bottom conductivity data of the electrical imaging logging to study the evaluation method of reservoir parameters.

3 Samples and methods

Tight carbonate reservoir is characterized by low degree of pores development, high degree of filling, various types of reservoir space, and complex pores structure (Rashid et al. 2015; Mahesar et al. 2020). For the porous reservoir, pores size distribution parameters and pores size spectrum calculation are done according to the electrical imaging bottom layer conductivity data matrix, to carry out quantitative calculation of reservoir parameters.

(1) Porosity calculation method

Conventional porosity calculation methods involve volumetric rock models and core calibration methods. The volume rock physics model aggregates the volumes of different rock components based on their physical property differences, ensuring that the total volume of the rock equals the sum of the volumes of each component. By establishing a logging response equation, porosity can be determined. The core calibration method, on the other hand, uses core calibration to establish the correlation between porosity and well logging curves, leading to the development of a porosity interpretation model. However, in the study area, the diversity of lithology makes the response value of the rock skeleton variable, rendering the former method unsuitable. Hence, in this study, a formation porosity calculation model was established by analyzing the
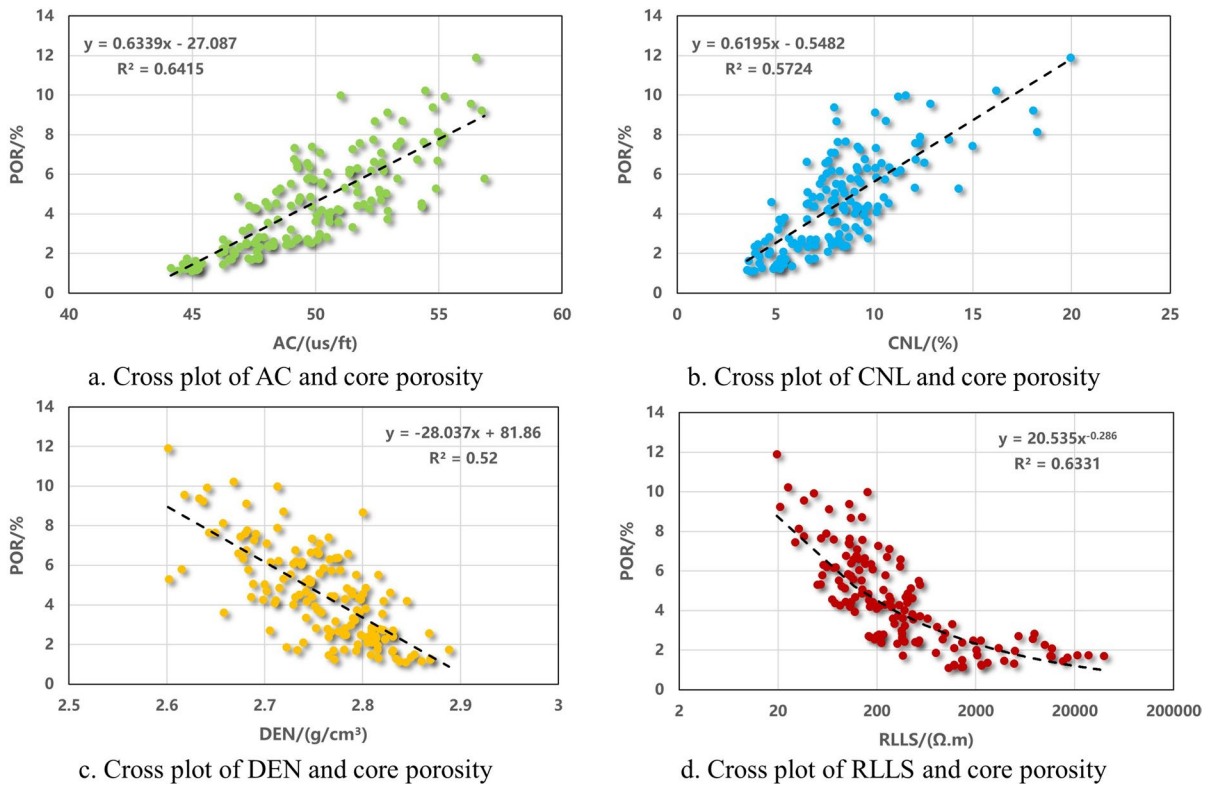

a. Cross plot of AC and core porosity

b. Cross plot of CNL and core porosity

c. Cross plot of DEN and core porosity

d. Cross plot of RLLS and core porosity

Fig. 6 Relationship between mean resistivity and porosity

correlation between conventional well logging curves and porosity (Fig. 6).

The correlation between well logging curves and core porosity is analyzed using cross plots (Fig. 6), and a model for explaining the porosity parameter is established through multiple regression. The multivariate fitting formula 1 is as follows:

$$\phi = 0.213*AC - 9.312*DEN + 0.231*CNL + 6.876*RLLS^{-0.136} + 11 \quad R^2 = 0.7932 \tag{1}$$

where ϕ represents the porosity interpreted from the well log, %; AC is a well logging curve represents the time it takes for sound waves to propagate within a unit distance in the formation, us/ft; DEN is a well logging curve characterizes the electron density index of the formation, g/cm^3; CNL is a well logging curve measures the ratio of thermal neutron count rates to characterize the hydrogen content of the formation,%; RLLS is a well logging curve focuses the power supply current radially towards the wellbore and measures the resistivity of the formation.$\Omega.m$;

(2)   Pores diameter calculation method.

Electrical imaging resistivity is determined by factors such as porosity, mud filtrate resistivity, and the degree of formation cementation. The degree of cementation is quantitatively characterized by the cementation index, which to some extent reflects the pore type, specifically the pore size.

By referring to Archie's empirical formula and the formation factor expression (2), an Eq. (3) can be derived that relates the cementation index to porosity, the resistivity of the formation in the shallow direction, and the resistivity of the mud filtrate. This equation can be generalized as the calculation Eq. (4) for the cementation index at each sampling point on the electrical imaging resistivity curve. In this equation, the resistivity of the electrical imaging logging represents the shallow lateral resistivity after scaling. Ultimately, the equation enables the calculation of the cementation index of the reservoir based on the electrical imaging resistivity curves.

$$F = \frac{R_o}{R_w} = \frac{a}{\phi^m} \tag{2}$$

$$m = \frac{log10(aR_{mf}) - log10(RLLS)}{log10(\phi)} \tag{3}$$

$$m_i = \frac{log10(aR_{mf}) - log10(R_i)}{log10(\phi)} \tag{4}$$

where F is stratigraphic factors, dimensionless; R_o is the Formation resistivity, $\Omega.m$; R_w is the Formation resistivity, $\Omega.m$; a is the cementation index, Generally the value is 1, dimensionless; ϕ is formation porosity, %; m is cementation index, dimensionless; R_{mf} is the mud filtrate resistivity, $\Omega.m$; $RLLS$ is the shallow lateral resistivity, $\Omega.m$; m_i is Calculated cementation index for each electroimaging sampling point, dimensionless; R_i is the Resistivity value at each electrical imaging sampling point, $\Omega.m$. i represents an index assigned to the sampling point of the electrical imaging well, ranging from 1 to 360.

The calculation steps of mud resistivity R_{mf} are as follows:

(1)   Calculate the mud resistivity at 18 degrees Celsius by Eq. (5):

$$R_{m18} = R_{m0} \times (1 + 0.023 \times (T_0 - 18)), \tag{5}$$

where R_{m18} is the resistivity of the mud at 18 °C, $\Omega.m$; R_{m0} is the resistivity of surface mud, $\Omega.m$; T_0 is the ground temperature, °C.

(2)   The mud resistivity under formation temperature is calculated by Eqs. (6 ~ 7):

$$T_1 = G \times Deep/100, \tag{6}$$

$$R_m = \frac{R_{m18}}{1 + 0.023 \times (T_1 - 18)}, \tag{7}$$

where T_1 is the formation temperature, °C; G is the isothermal gradient; Deep is the depth of the well, m; R_m is the resistivity of mud, $\Omega.m$;

(3)   Calculation of the mud filtrate resistivity by Eq. (8)

$$R_{mf} = C \times R_m^{1.07}, \tag{8}$$

(4)   The coefficient C in Eq. (9) is calculated by mud density using the equation

Table 1 Statistical comparison of core experimental data and well logging calculation of m

| Well | Depth (m) | Physical | | m by Cal | Pores diameter | Cast thin slices | Mercury injection |
| | | POR | PERM | | | Average pores diameter | Average pores diameter |
		(%)	$(10^{-3}\mu m^2)$		μm	μm	μm
M128	2063.6	2	0.023	2.5	3.4	/	3.4
M128	2066.75	5.7	9.29	3.34	1.5	/	1.5
J18	3383.35	11.6	0.398	2.59	5.96	/	5.96
J18	3383.6	11.8	6.83	3.14	4.81	/	4.81
T85	3240.58	19.4	5.16	2.02	50.58	/	/
T105	3680.88	9.3	170	1.86	281.62	/	/
T105	3681.2	7.2	15.7	1.78	90.72	/	90.72
L108	3966.85	5.3	0.631	1.9	140	140	/
S474	3535.4	8.7	4.26	2.09	9.21	/	9.21
S474	3535.8	7.7	1.43	1.79	48.07	/	48.07
L108	3967	5.8	4.54	1.64	345.98	345.98	/
T105	3681.4	6.9	8.65	1.82	399.7	399.7	/
J9	3612.92	6.3	3.83	1.89	160	160	/
L108	3847	9.5	0.142	1.43	280	280	/
L108	3814.22	11.1	3.78	2.29	85	/	85
S474	3536.4	4.3	0.051	1.6	400	400	/
L35	3713.9	13.6	6.39	1.83	2150	2150	/
L35	3714.1	8.2	8.05	1.8	800	800	/
T85	3242.9	13.1	8	1.45	1000	1000	/
T85	3243.1	14.7	2.79	1.54	240	240	/
T85	3248	13.7	4.3	1.58	40	/	40
T85	3250.5	6.1	0.078	1.97	20	/	20

$$C = 0.769 \times DEN_m^2 - 3.086 \times DEN_m + 3.437, \qquad (9)$$

where DEN_m is the mud density measured on the ground, g/cm^3.

Based on our geological understanding of the pore structure in the tight carbonate reservoir of the Ordos Basin, combined with the characteristic observation scales of the mercury intrusion experiment and cast thin section experiment, different experimental data scales were selected for different pore size ranges. The mercury intrusion experiment primarily reflects pore sizes below 100 microns. Hence, the pore size distribution statistics from the mercury injection experiment were utilized to calculate the average pore radius scale for pores with diameters below 100 microns.

On the other hand, the cast thin section observation scale operates at the micrometer to millimeter level. The pore size scale derived from the cast thin
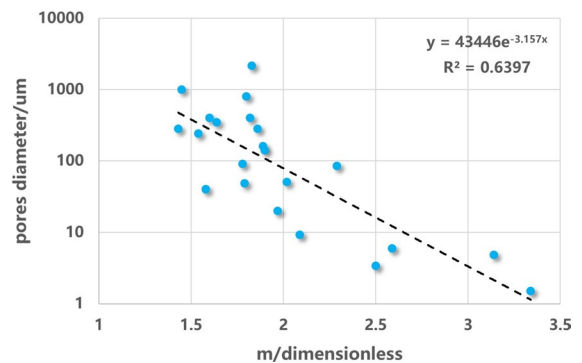

Fig. 7 Relationship between m and pores diameter

section data is set at 100 microns. For pores falling within this range, the statistical table provided in the article helps calculate the cementation index and pore diameter. The porosity grade permeability displayed

in the table is based on core experimental data (Table 1), while the pore radius is a comprehensive value derived from experimental data and reservoir knowledge. If the pore diameter exceeds 100 microns, the experimental data from the cast thin section will be utilized. Conversely, for pore diameters less than 100 microns, the experimental data from the mercury intrusion will be employed.

Based on the data provided in the table, a statistical analysis was conducted to examine the relationship between the cementation index calculated from well logging and the pore size data obtained from core experiments. A cross-plot diagram was generated as shown in Fig. 7. The resulting analysis revealed a consistent negative correlation between the cementation index and pore size. In other words, as the cementation index increases, the size of the formation pores decreases.

By further analyzing the correlation depicted in the cross-plot diagram, a pore size interpretation model was established by Eq. (10) for the reservoir within the Ma5 Member in the eastern paleo-uplift:

$$D_p = 43446e^{-3.157m}, R^2 = 0.6397, \tag{10}$$

where D_p is the pores diameter, μm; m_i is Calculated cementation index, dimensionless.

The aforementioned relationship was extended to encompass the calculation of electrical imaging data, with the revised formula expressed as Eq. (11):

$$D_p^i = 43446e^{-3.157m_i}, R^2 = 0.6397, \tag{11}$$

where D_p^i is the pores diameter for each electroimaging sampling point, μm; m_i is Calculated cementation index for each electroimaging sampling point, dimensionless.

Table 2 Statistical table of pores diameter and carbonate reservoir space

Intervals/um	Index	Range name	Pores diameter range/um	Pores subclass	Pores type
$10^{-1} \sim 10^0$	1	R_1	0.1~0.16	Micro pores	Pores
	2	R_2	0.16~0.25		
	3	R_3	0.25~0.4		
	4	R_4	0.4~0.63		
	5	R_5	0.63~1		
$10^0 \sim 10^1$	6	R_6	1~1.58		
	7	R_7	1.58~2.51		
	8	R_8	2.51~3.98		
	9	R_9	3.98~6.31		
	10	R_{10}	6.31~10		
$10^1 \sim 10^2$	11	R_{11}	10~15.85	Small pores	
	12	R_{12}	15.85~25.12		
	13	R_{13}	25.12~39.81		
	14	R_{14}	39.81~63.1		
	15	R_{15}	63.1~100		
$10^2 \sim 10^3$	16	R_{16}	100~158.49	Medium pores	
	17	R_{17}	158.49~251.19		
	18	R_{18}	251.19~398.11		
	19	R_{19}	398.11~500		
	20	R_{20}	500~1000	Coarse pores	Hole
$10^3 \sim 10^4$	21	R_{21}	1000~1584.89		
	22	R_{22}	1584.89~2000		
	23	R_{23}	2000~3981.07	Hole	
	24	R_{24}	3981.07~6309.57		
	25	R_{25}	6309.57~10,000		

Input: D_p^i, the pores diameter for each electroimaging sampling point; R_j, the pores diameter range , j=1,2,…,25.

Output: D_j, Interval-fixed pore diameter statistics, j=1,2,…,25; ϕ_k, Pore categories corresponding to different subcategories of pores, k=1,2,…,5.

1   if $D_p^i \in R_j$:
2           $D_j = D_j +1$
3   if $D_p^i \in R_1 \sim R_{10}$:
4           $\phi_1 = \phi_1 +1$
5   if $D_p^i \in R_{11} \sim R_{15}$:
6           $\phi_2 = \phi_2 +1$
7   if $D_p^i \in R_{16} \sim R_{19}$:
8           $\phi_3 = \phi_3 +1$
9   if $D_p^i \in R_{20} \sim R_{22}$:
10          $\phi_4 = \phi_4 +1$
11 if $D_p^i \in R_{23} \sim R_{25}$:
12          $\phi_5 = \phi_5 +1$
13 $D_j = D_j / \phi$
14 $\phi_k = \phi_k / \phi$
Final;
Return D_j , ϕ_k

Fig. 8 Flowchart for calculating pore spectrum and pore component

(3)   Calculation method of pores diameter spectrum.

From the Eq. (10), 360 pores diameters can be calculated for each depth point to obtain the pores diameter matrix data of the whole well section. However, we prefer to study the difference between pores size distribution instead of the pores data matrix. Therefore, the pores data is divided into five intervals: $10^{-1} \sim 10^0$、 $10^0 \sim 10^1$、 $10^1 \sim 10^2$、 $10^2 \sim 10^3$、 and $10^3 \sim 10^4$. Further, each interval is divided into five intervals, resulting to 25 intervals, which are divided to count 360 pores diameter data. See Table 2 for the specific division rules of the interval.

To compare the pores diameter distribution between different depths, divide the above statistics by the sum to get the pores diameter distribution component of each interval. The pores size spectrum is the distribution range of pores diameter and the pores component of each pores size range. Based on the pores size spectrum, the component porosity of five types of pores are obtained by counting the porosity of micro-pores, fine pores, medium pores, coarse pores, and pores diameter interval. These five types of pores are classified according to the pores diameter in the industry standard of cast thin section identification.

If the pores size distribution component is multiplied by pores, the sum of each interval is porosity (decimal), and the value of each interval is porosity component. The flowchart for calculating pore diameter and pore component is outlined as follows (Fig. 8):

(4)   Calculation of permeability by pores composition method.

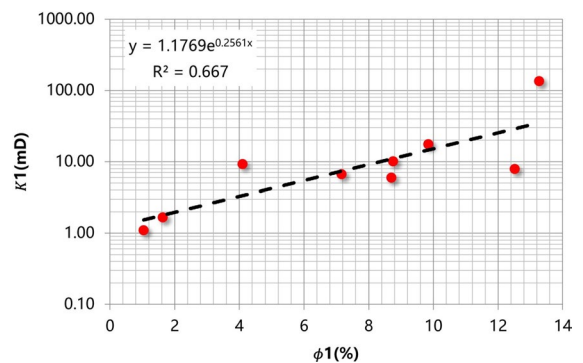Tight carbonate reservoirs in Ordos Basin can increase pores diameter and throat width. The

Fig. 9 Relationship between porosity and permeability of coarse pores and hole rock sample
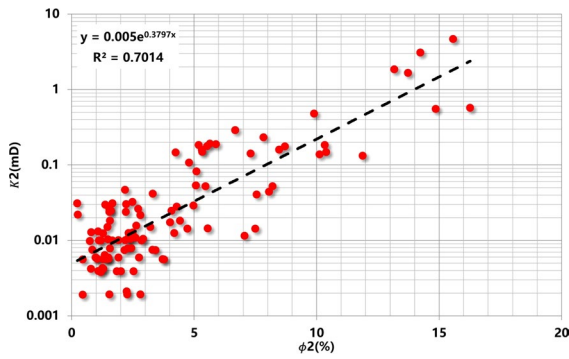
Fig. 10 Relationship between porosity and permeability of medium pores and small pores

permeability contribution rate of different pores components is unique. The hole contribution rate is high, whereas the micropores contribution rate is low. The larger the pores size, the greater the permeability contribution. Therefore, the relationship between porosity and permeability of different pores components can be established, and the reservoir permeability can be calculated by linear combination (Fig. 9).

Further, the vuggy reservoir is developed in Mawu on the east side of paleo uplift. The rock samples of vuggy reservoir are selected to analyze the porosity and permeability, while the porosity permeability relationship of vuggy reservoir is established as the relationship of coarse porosity & hole and permeability.

The relationship between permeability and porosity of coarse pores & hole is as follows:

$$K_1 = 1.1769e^{25.61\phi_1}, R^2 = 0.667, \tag{12}$$

where, ϕ_1 is the porosity of coarse pores and hole, %; K_1 is the permeability partly contributed by the coarse pores and hole, mD.

Furthermore, intergranular porosity reservoir is developed in Mawu reservoir in the east of paleo uplift. Rock samples of intergranular porosity and intergranular solution porosity reservoir are selected to analyze porosity, permeability, and establishes porosity permeability relationship, which is regarded as porosity permeability relationship of medium pores and small pores, as shown in Fig. 10.

The relationship between the permeability and medium pores and small pores is as follows:

$$K_2 = 0.0049e^{38.194\phi_2}, R^2 = 0.4509, \tag{13}$$

where, ϕ_2 is the porosity of medium pores and small pores, %; K_2 is the permeability, partly contributed by the medium pores and small pores, mD.

The contribution of micropores porosity to permeability is below 0.05 mD, which is low. So, the contribution of micropores porosity to permeability is not considered.

Therefore, the formula for the component porosity and the permeability is

$$K = 0.005e^{37.68*\phi_2} + 1.1769e^{25.61*\phi_1}, \tag{14}$$

where K is the reservoir permeability, mD.

4 Results and discussions

4.1 Analysis of calculation results

According to the calculation results, the porosity development degree of dolomite vuggy reservoir in Ordos Basin is relatively good. Thus, Ma five member of JIN x well is taken as the error analysis layer. The porosity is mainly distributed in 2% ~ 4%, with an average of 3.51%. The comparison between the porosity calculated using the average resistivity of electrical
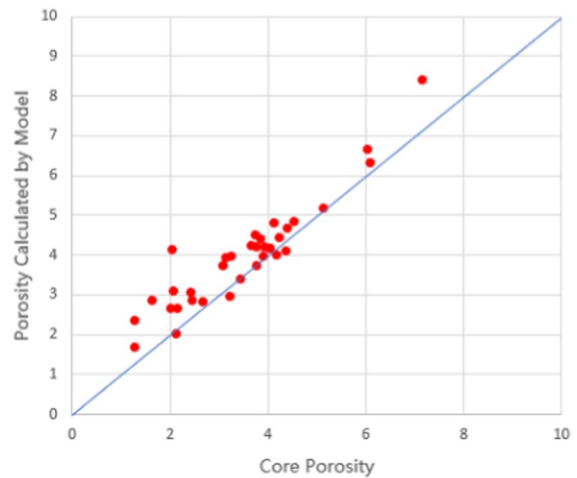

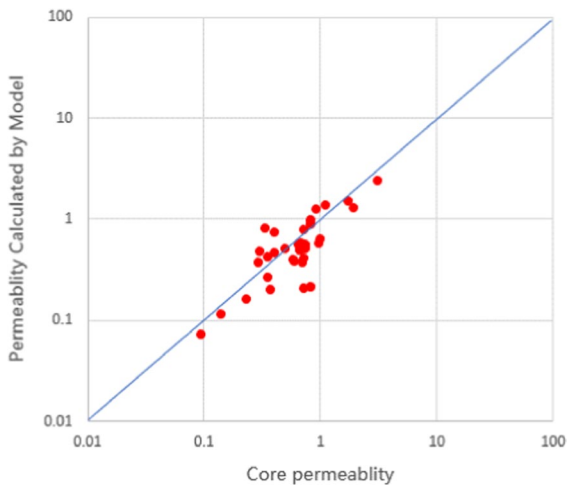**Fig. 11** Porosity error analysis chart

Fig. 12 Permeability error analysis

imaging and that of core analysis, is shown in Fig. 11. It can be seen from the cross plot that the two are basically consistent, and most of the porosities are within one porosity error. From the error distribution, the porosity error of 90% sample points is less than 1%, and the average porosity error is 0.905 p.u (Fig. 12).

4.2 Application examples

To further verify the effectiveness of the evaluation of the parameters of dense carbonate reservoir based on the borehole spectrum of electrical imaging logging, this paper makes a comprehensive analysis of the Ma five formation section of JIN X well in the research area. The comprehensive analysis chart of the calculation results of reservoir parameters (Fig. 13) is divided into seven. The first is the original static electrical imaging diagram. The second is the static map of the whole borehole coverage of electric imaging made by Schlumberger techlog software, while the third is the uranium degasification gamma curve. The fourth is the weighted average of pores size calculated using pores size spectrum and pores distribution. The fifth is the porosity component calculated using pores size spectrum. The sixth is the comparison channel between the porosity calculated using the model and the porosity of core analysis, and the seventh is the comparison channel of model calculation permeability and permeability of core analysis.

From the electrical imaging pictures, it can be seen that the lithology of this section is dense, without
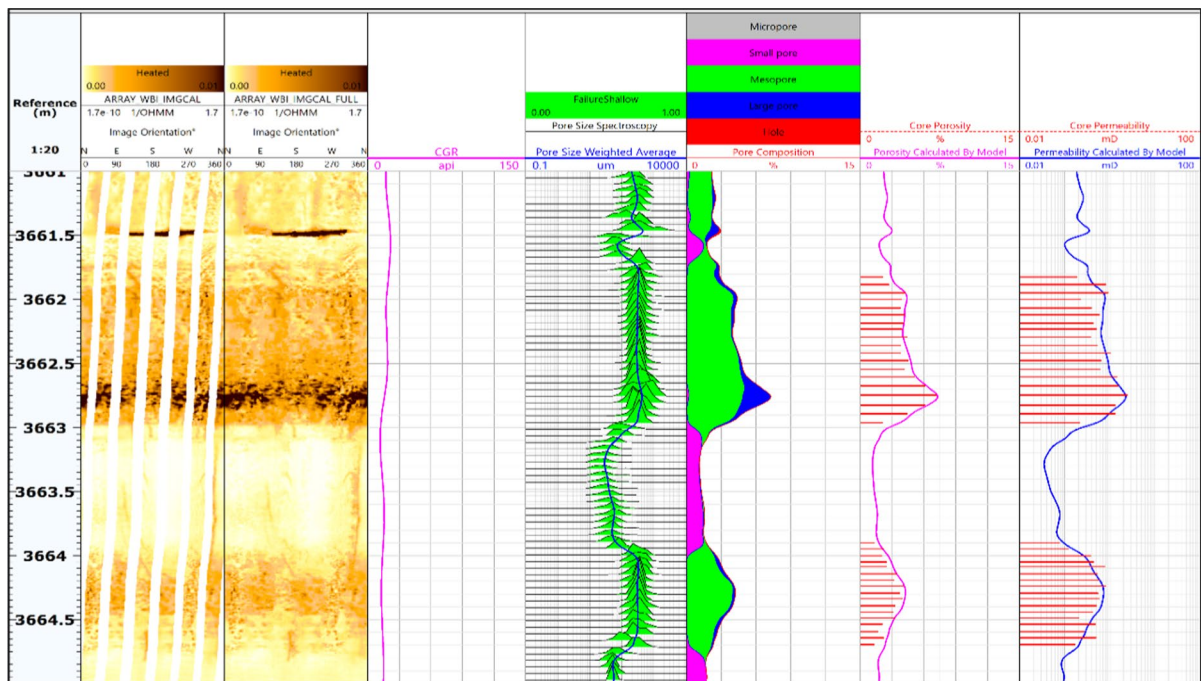
Fig. 13 Electric imaging interpretation map of Ma 5 layer in Jin x well

obvious holes, and there may be high angle microfractures at the depth of 3663.5~3664.5 m. The de uranium gamma curve shows that the shale content in this section is less. The aperture spectrum has a logarithmic trace, where the scales at both ends are 0.1um and 10,000 um, respectively. The height of the aperture spectrum indicates the frequency of the aperture curve, and the blue curve is the weighted average of the aperture. Figure 13 shows that the aperture is mainly distributed between 10 and 1000 um, though some aperture distribution is greater than 1000 um at some depths. According to the porosity component trace, the main types of pores in this section are meso-pores and micro-pores, with a small number of coarse-pores and macro-pores; The porosity calculated by the model is higher than that of the core analysis. The possible reason is that the isolated pores are not considered in the core analysis, but on the whole, the porosity calculated using the model is basically the same as that of the core analysis. The core analysis permeability of 3661.8~3662.9 m section is lower than that calculated using the model, but the core analysis permeability of 3663.9~3664.7 m section is higher than that calculated using the model, which may be that the effect of microfracture on permeability is not considered in the model.

5 Conclusions

For carbonate rock reservoirs, particularly those with complex and dense pore structures, the permeability of the reservoir not only affects the effectiveness of fracture construction, but also impacts reservoir productivity. Accurate evaluation of penetration parameters is therefore crucial for well interpretation. In this article, the author demonstrates that the proposed method effectively evaluates pore structure parameters in dense carbonate reservoirs. The main innovation of this method lies in establishing a calculation approach for pore spectrum and different pore types based on the resistivity curve from electrical imaging.

The process begins with the scale of mercury pressure compression experiments at the nano-micron level, which establishes the relationship between tuning index well measurements and apertures below 100 microns. Through casting slices at the micron to millimeter scale, the relationship between the cementation index and pore diameter of 100 μm is

determined. This forms the basis for calculating pore diameter, which then allows for statistical analysis and distribution profiling.

The established pore structure parameters and diffusion calculation model yielded relative errors within 90% when compared to experimental data from rock cores. This meets the criteria of standard interpretation. The proposed method in this article solely considers the correlation among simple parameters, without incorporating additional conditions. Readers can further explore other non-linear mapping relationships between pore structure and reservoir penetration, as well as study the distribution of reservoir fluids in conjunction with nuclear magnetic test wells. Improved accuracy in explaining unconventional reservoirs with acidic rocks will provide robust support for oil and gas exploration and production.

Declarations

References

Chen YX et al (2020) Effectiveness evaluation method for tight carbonate reservoirs based on electrical imaging logging data. Well Logg Technol 44(01):49–54

Chitale DV, Quirein J, Perkins T, et al (2004) Application of a new borehole imager and technique to characterize secondary porosity and net-to-gross in vugular and fractured carbonate reservoirs in Permian Basin. In: SPWLA 45th Annual Logging Symposium. Society of Petrophysicists and Well-Log Analysts, 2004.

Chong F, Qingbin W, Zhongjian T et al (2019) Logging classification and identification of complex lithologies in volcanic debris-rich formations:an example of KL16 oilfield. Bsin Acta Petrolei Sinica 40(S2):91–101

Feng CW (2019) Logging classification and identification of complex lithologies in volcanic debris rich formations: anexample of KL16 oilfield. ActaPe troleiSinica 40(S2):91

Haizhou QU, Zhang F, Zhenyu W et al (2016) Quantitative fracture evaluation method based on core-image logging: a case study of Cretaceous Bashijiqike Formation in ks2 well area, Kuqa depression, Tarim Basin. NW China Petrol Expl Devel 43(3):465–473

Jianping Y, Jingong C, Minghai Z et al (2011) Application of electrical image logging in the study of sedimentary characteristics of sandy conglomerates. Pet Explor Dev 38(4):444–451

Jingli Y, Xiuqin D, Yande Z et al (2013) Characteristics of tight oil in Triassic Yanchang formation. Ordos Basin Petrol Explor Devel 40(2):161–169

Jinhua F, Liyong F, Xinshe L et al (2019) New progresses, prospects and countermeasures of natural gas exploration in the Ordos Basin. China Petrol Explor 24(4):418

Khoshbakht F, Azizzadeh M, Memarian H et al (2012) Comparison of electrical image log with core in a fractured carbonate reservoir. J Petrol Sci Eng 86:289–296

Liu S (1998) The coupling mechanism of basin and orogen in the western Ordos Basin and adjacent regions of China. J Asian Earth Sci 16(4):369–383

Mahesar AA, Shar AM, Ali M et al (2020) Morphological and petro physical estimation of eocene tight carbonate formation cracking by cryogenic liquid nitrogen; a case study of Lower Indus basin, Pakistan. J Petrol Sci Eng 192:107318

Rashid F, Glover PWJ, Lorinczi P et al (2015) Porosity and permeability of tight carbonate reservoir rocks in the north of Iraq. J Petrol Sci Eng 133:147–161

Safinya KA, Le Lan P, Villegas M, et al (1991) Improved formation imaging with extended microelectrical arrays. In: SPE Annual technical conference and exhibition. OnePetro

Wu YY, Zhang WM, Tian CB et al (2013) Application of image logging in identifying lithologies and sedimental facies in reef-shoal carbonate reservoir—Take Rumaila oil field in Iraq for example. Prog Geophys 3:44

Xu F, Wang Z, Wang W (2021) Evaluation of fractured–vuggy reservoir by electrical imaging logging based on a denoising method. Acta Geophys 2021:1–12

Yang Y, Li W, Ma L (2005) Tectonic and stratigraphic controls of hydrocarbon systems in the Ordos basin: a multicycle cratonic basin in central China. AAPG Bull 89(2):255–269

Zhang ZH, Du SK, Chen HY et al (2018) Quantitative characterization of volcanic fracture distribution based on electrical imaging logging: a case study of Carboniferous in Dixi area, Junggar Basin. Acta Petrolei Sinica 39(10):1130–1140